The Effective Behaviour of Linear and Nonlinear Waves in Irregular Channels

By ANDRÉ NACHBIN

Instituto de Matemática Pura e Aplicada, Estrada D. Castorina, 110, Rio de Janeiro, RJ, CEP 22460-320, Brazil, nachbin@impa.br

A fluid mechanics model is built in several stages. The passage from a simplified, prototypical model to a more sophisticated one leads to a natural question: will given properties be preserved by the more complex model? Linear potential theory is taken to be our reduced/prototypical model for water wave propagation. The hydrostatic Navier–Stokes equation is chosen as the nonlinear, more sophisticated, model. It is shown to be a consistent limiting model for reflection–transmission problems in the presence of rapidly varying topographies. The persistence of linear potential theory results are verified for surface pulse propagation in the presence of both periodic and disordered topographies. Numerical experiments show that effective behaviour is preserved. In particular, waves propagating over large amplitude, rapidly varying topographies do not break. Stochastic theory results from linear potential theory are validated with the nonlinear numerical model. This corroborates linear theory. Additional wave–topography experiments are performed beyond the regime of validity of linear potential theory. Nonlinear waves, bores and viscous flows are considered. These new results include the delay of bores by rapidly varying topographies. Evidence is given that apparent diffusion, due to disordered topographies, can dominate viscous diffusion.

1. Introduction

Surface wave interaction with submerged topographies can be analyzed through different models. The choice of a specific model is usually motivated by its ability to capture a given phenomenon. For instance, in some cases sediment transport along the bottom is of primary interest. Alternatively, in other models attention is focused along the free surface where details of the flow near the bottom might not be so important.

This work is in the spirit of modelling in water wave propagation. Surface wave interaction with a submerged topography has been analyzed in several different ways. Among others, Devillard *et al.* (1988) and Evans & Linton (1994) considered potential theory as a model for wave–topography interaction, while Belzons *et al.* (1988) and Rey *et al.* (1992) performed laboratory experiments validating potential theory. Another viewpoint of potential theory is presented in Nachbin & Papanicolaou (1992b), where the reflection–transmission problem is studied in the case of large amplitude, rapidly varying, disordered topographies. The asymptotic theory developed there makes use of stochastic differential equations. The corresponding numerical experiments were performed with the boundary element method. The comparison between theory and computations can be found in Nachbin & Papanicolaou (1992a, 1992b), Nachbin (1993) and Nachbin (1995). The agreement is very good but linear potential theory has limitations. Nevertheless, it is an excellent tool in revealing some fundamental aspects of the wave–topography interaction.

A typical modelling question arises: which results will persist for a more complete model? To address this question, a nonlinear model is chosen and its linear regime identified. We show that linear potential theory has many essential ingredients for understanding long surface wave interaction with a rigid, impermeable bottom. In particular, potential theory is a useful mathematical tool to analyze how rapidly varying geometric features of the topography affect a long wave along the free surface. From the modelling side we look at linear potential theory as a reduced model. As the more sophisticated model we choose the hydrostatic Navier–Stokes equation (HNS). We start by showing how a hydrostatic model is consistent with the reflection–transmission problem studied. We verify the persistence of linear potential theory results using this nonlinear model. As we succeed with the verification experiments, we perform numerical simulations beyond the regime of validity of linear potential theory. New results are obtained. Both nonlinear waves and viscous flows are considered.

Within the scope of linear potential theory the following questions are posed in this paper:

(i) Will the HNS model respond adequately to the classical scaling of potential theory?

(ii) Will *effective media properties* persist under the HNS simulations? How far can we go before nonlinearity plays a role in the reflection–transmission problem?

(iii) Will large amplitude, rapidly varying topographies induce wave breaking? Note that linear potential theory can not capture wave breaking.

(iv) Can the wave attenuation due to viscosity be dominated by the apparent attenuation due to disorder?

The apparent attenuation due to multiple disordered scattering was first studied in the context of acoustic waves (c.f. Asch *et al.* 1991, Richards & Menke 1983). We will discuss this issue in more detail.

Positive answers to **(i)** and **(ii)** validate potential theory. In fact, for small values of the amplitude/depth ratio (of the order of 10^{-3}) we observe linear advection of the free surface pulse. When the ratio reaches 0.1 a smooth pulse becomes a bore after the time interval predicted by Burgers equation. The regime is clearly nonlinear. When the channel is rough and the amplitude/depth ratio is small, the nonlinear model reproduces linear potential theory results. When the scaling parameter goes beyond the linear regime we observe new results such as the delay of bores in the presence of rapidly varying periodic topographies. The bore shape is unchanged and no reflection is generated. We also show that the stochastic theory, given in Nachbin & Papanicolaou (1992b) and Nachbin (1995), coincides with the numerical Monte Carlo simulations for pulses beyond the linear regime. As the wavefront steepens it interacts more strongly with the fine features of the topography and generates a reflected signal with more structure.

Questions **(iii)** and **(iv)** address other issues that have not been explored before. The HNS model captures both linear advection as well as wave breaking into bores. A fundamental result is obtained, corroborating linear theory: large amplitude, rapidly varying topographies will not induce wave breaking. The pulse is wide with respect to the fine features of the topography and therefore an averaging mechanism takes place. We also show that the apparent wave attenuation due to disorder can dominate the attenuation due to viscosity. The apparent attenuation, due to the fine features of the topography, will also be called apparent diffusion. We will explain the connection between disordered multiple scattering and a diffusive–like mechanism.

The paper is organized as follows. In section 2 we present the full nonlinear potential theory model. A summary of results is presented in the appendix. For irregular channels with periodic topographies we briefly describe the multiscale asymptotic analysis developed by Rosales & Papanicolaou (1983). We also describe the relevant results when the

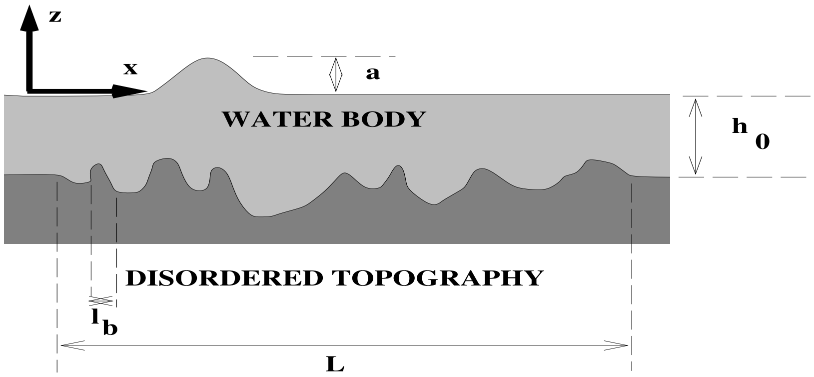

FIGURE 1. Typical geometry for a disordered channel.

waves are linear and the topography is disordered. These are derived from the application of an asymptotic theory for the solution of stochastic differential equations (Nachbin & Papanicolaou 1992b).

In §3 we establish the connection between the potential theory reflection–transmission problem and the hydrostatic (shallow water) reflection–transmission problem, for the specific case of rapidly varying topographies.

The three dimensional hydrostatic Navier–Stokes model is described in §4. The numerical method used in our simulations is due to Casulli & Cheng (1992). It is a semi–implicit, semi–Lagrangian finite difference discretization of the hydrostatic Navier–Stokes equations.

In §5 we present a series of numerical experiments for the inviscid regime. The model reduces to the nonlinear Shallow Water Equations. The goal is to address the same questions as we did with the one–dimensional boundary element experiments in Nachbin & Papanicolaou (1992a, 1992b) and Nachbin (1995). We start with scaling experiments, in a flat channel, to identify the effective linear regime of the nonlinear model. Experiments are then performed with both periodic and disordered topographies. Nonlinear wave simulations are also analyzed.

In §6 viscosity is considered. The main goal is to compare the viscous attenuation of propagating pulses with the apparent attenuation due to the disordered medium. The conclusions are given in §7.

2. Formulation and background for the potential theory model

Consider gravity driven surface waves, propagating in shallow channels, in a regime where potential theory is applicable. Namely, the fluid is taken to be inviscid, incompressible and the flow is irrotational. The velocity potential $\phi(x,z,t)$ satisfies the equation (given in dimensionless variables (Whitham 1974))

$$\beta\ \phi_{xx} + \ \phi_{zz} \ = \ 0, \quad \text{with} \quad -\ h(x/\gamma) < z < \alpha\ \eta(x,t),$$

defining the corrugated strip representing the channel. A typical channel with a disordered topography profile $h(x/\gamma)$ is shown in figure 1. The dimensionless parameters α, β and γ are defined below. The nonlinear boundary conditions at the unknown free surface elevation $z = \alpha\ \eta(x,t)$ are: the kinematic condition

$$\eta_t + \alpha\ \phi_x \eta_x - \frac{1}{\beta}\phi_z = 0, \quad \text{on} \ \ z = \alpha\ \eta(x,t)$$

and the Bernoulli law (dynamic condition)

$$\eta + \phi_t + \frac{\alpha}{2}\left(\phi_x^2 + \frac{1}{\beta}\phi_z^2\right) = 0, \quad \text{on} \ \ z = \alpha\ \eta(x,t).$$

At the impermeable bottom we impose the homogeneous Neumann condition

$$\frac{d\phi}{dn} \equiv \phi_z + \frac{\beta}{\gamma}\ h'(x/\gamma)\phi_x = 0 \quad \text{along} \ \ z = -\ h(x/\gamma).$$

The initial conditions at the free surface are:

$$\phi(x,0,0) = \phi_0(x) \qquad \text{and} \qquad \phi_t(x,0,0) = \phi_1(x).$$

The bottom topography described by $z = -h(x/\gamma)$ is such that

$$h(x/\gamma) \ \ = \ \ \begin{cases} 1 - n(x/\gamma) & \text{when} \ \ -L < x < 0 \\ 1 & \text{when} \ \ x \leq -L \ \ \text{or} \ \ x \geq 0. \end{cases}$$

We have introduced the scales for the typical depth h_0, typical wavelength λ, typical amplitude a of the free surface elevation $\eta(x,t)$, horizontal length scale l_b of the bottom irregularities and L the total length of the rough region. When using dimensionless variables the following dimensionless parameters appear: $\alpha = a/h_o$, controlling the strength of the nonlinearity, $\beta = h_0^2/\lambda^2$, which controls dispersion and $\gamma = l_b/\lambda$, which indicates how rapidly the bottom irregularities vary. The acceleration due to gravity is denoted by g and the reference shallow water speed is $c_0 = \sqrt{gh_0}$. We denote by $n(x/\gamma)$ the inhomogeneities about the undisturbed bottom at depth $z = \ -1$, and it can be a periodic or random function. Note that the depth fluctuations $n(x/\gamma)$ are not necessarily small. Regimes of interest can be identified by expressing the dimensionless parameters in terms of a small parameter $\varepsilon > 0$ (see Nachbin 1993; Whitham 1974).

Regarding the theory developed in Nachbin & Papanicolaou (1992b), we have ordered the length scales in such a way that disorder varies on the same length scale as the depth. We call it the microscopic scale and it is $O(1)$. We want the waves to be long enough so that they feel the disordered topography in some averaged form. The wavelength, in the time harmonic case, or the pulse width, scales like $1/\varepsilon$. We call this the intermediate scale. Finally, we are interested in regimes where the waves must interact with the rough bottom topography over large distances. We call this the macroscopic scale and it is $O(1/\varepsilon^2)$. From Mei's book (Mei 1983), we see that these are typical scales for a tsunami wave propagating over the continental shelf.

In the appendix we summarize the potential theory results of interest.

3. The effectively hydrostatic ensemble–averaging limit

The stochastic reflection–transmission theory presented in Nachbin & Papanicolaou (1992b) is reviewed from a slightly different perspective. Our goal is to motivate the use of the hydrostatic Navier–Stokes model given in the next section.

In the introduction of Nachbin & Papanicolaou (1992b) it has been pointed out that the shallow water equations are not valid as an asymptotic approximation *at the level of equations*, when the topography is rapidly varying. This motivated the stochastic analysis with the linear potential theory equations, in the shallow water (long wave) regime. Nevertheless we observe, at the end of the time harmonic asymptotic analysis, that the evanescent modes play no role in the ensemble–averaging characterization of the reflection-transmission coefficients. The associated diffusion equation is basically the same as the one obtained for the acoustic wave equations. This conclusion led to the use of a specific stochastic wave model for the analysis of pulse shaped waves (c.f. equations (50)-(52) in Nachbin & Papanicolaou 1992b). The only aspect that would not have been captured, had we used the shallow water equations directly, is the topography-smoothing effect, expressed through the "variable free surface coefficient" m(x), and the depth parameter γ_h both defined in the appendix of the present article.

To make this clear, we review part of the theory presented in Nachbin & Papanicolaou (1992b) in a different, more detailed, fashion. The same notation is used. Define the reflection matrix $\mathbf{Z}$ from the relation

$$[A_0(x)...A_j(x)...]^T \;=\; \mathbf{Z}(x)\,[B_0(x)...B_j(x)...]^T \quad j = 0, 1, \ldots,$$

where $A_0(x)$ and $B_0(x)$ are the amplitudes of the right and left propagating modes. The amplitudes of the evanescent modes are denoted by $j \geq 1$. Over the disordered region $-L \leq x \leq 0$ it satisfies the matrix Riccati equation

$$\frac{d\mathbf{Z}}{dx} \;=\; \mathbf{DZ} + \mathbf{ZD} + \mathbf{M}_{11}\mathbf{Z} + \mathbf{M}_{12} - \mathbf{ZM}_{21}\mathbf{Z} - \mathbf{ZM}_{22} \tag{3.1}$$

with $\mathbf{Z}(-L) = 0$. The matrizes $\mathbf{M}_{ij}$ and $\mathbf{D}$ are given in detail in Nachbin & Papanicolaou (1992b) and Nachbin (1993).

Waves are incident from the right and $Z_{00}(0)$ leads to the reflection coefficient. The stochastic Riccati equation (3.1) is analyzed in the long wave limit as ε tends to zero. In this limit, the coefficient $m(x/\varepsilon^2)$ is considered to be a stationary stochastic process with given properties. For the coefficient of interest Nachbin & Papanicolaou (1992b) derived the stochastic differential equation

$$\frac{d}{dx}Z_{00} \;=\; \frac{i\omega}{\varepsilon}\left(\frac{m(x/\varepsilon^2)}{2\gamma_h}\right)\left[2Z_{00} + e^{i\omega x/\varepsilon}\sum_{j=1}^{\infty}(-1)^j Z_{j0} + e^{2i\omega x/\varepsilon} + \right. \tag{3.2}$$

$$\left. + Z_{00}\left(Z_{00}e^{-2i\omega x/\varepsilon} + e^{-i\omega x/\varepsilon}\sum_{j=1}^{\infty}(-1)^j Z_{j0}\right)\right] + O(1)(\text{mean zero term}).$$

The terms omitted are of order one relative to ε and have zero mean, so that they do not contribute in the ensemble–averaging limit. The vector field for this equation depends only on the entries of the first column of $\mathbf{Z}$. These are the only (evanescent mode dependent) entries that can couple with Z_{00} in the asymptotic analysis.

Several limiting coefficients are computed for the associated diffusion theory. It works out that the evanescent Z_{j0} components do not contribute to the statistics of Z_{00}. Thus we can restrict ourselves to the equation for Z_{00} alone, with all the Z_{j0}'s in it equal to zero. Namely

$$\frac{d}{dx}Z_{00} \;=\; \frac{i\omega}{\varepsilon}\left(\frac{m(x/\varepsilon^2)}{2\gamma_h}\right)\left[2Z_{00} + e^{2i\omega x/\varepsilon} + Z_{00}^2 e^{-2i\omega x/\varepsilon}\right]. \tag{3.3}$$

It should be emphasized that the asymptotic negligibility of the evanescent modes is true only when there are no deterministic discontinuities in the bottom topography, as we have assumed here.

The stochastic differential equation (3.3) governs the reflection process in the limit when the disordered features of the topography are on an infinitesimal scale when compared to the wavelength. These equations are exactly the same as those derived by Burridge *et al.* (1989) for acoustic waves in a randomly layered half space ($x < 0$). Let the velocity be given by $u(x,t)$ and the pressure by $p(x,t)$. The acoustic problem is governed by the system

$$\rho(x)\frac{\partial u}{\partial t} + \frac{\partial p}{\partial x} = 0 \tag{3.4}$$

$$\frac{1}{K(x)}\frac{\partial p}{\partial t} + \frac{\partial u}{\partial x} = 0,$$

where ρ is the density and K the bulk modulus. Burridge *et al.* (1989) allowed for disorder in both the density and bulk modulus. Their reflection process R^ε is governed by (equation (2.31) in Burridge *et al.* 1989):

$$\frac{d}{dx}R^\varepsilon = \frac{i\omega}{\varepsilon}\left(\frac{\rho_0(x)}{K_0(x)}\right)^{1/2}\left[n^\varepsilon e^{2i\omega\tau(x)/\varepsilon} + 2m^\varepsilon R^\varepsilon + n^\varepsilon (R^\varepsilon)^2 e^{-2i\omega\tau(x)/\varepsilon}\right] +$$

$$+\frac{1}{4}\frac{(\rho_0(x)K_0(x))'}{\rho_0(x)K_0(x)}\left[e^{2i\omega\tau(x)/\varepsilon} - (R^\varepsilon)^2 e^{-2i\omega\tau(x)/\varepsilon}\right],$$

with the travel time

$$\tau(x) = \int_x^0 \frac{ds}{c_0(s)}.$$

The notation is such that the propagation speed $c_0(x) \equiv (K_0(x)/\rho_0(x))^{1/2}$ depends only on the slow background variation of the density and bulk modulus. The random coefficients m^ε and n^ε depend on the disorder of both the density and the bulk modulus.

Consider the specific case where there are no background variations (i.e. ρ_0 and K_0 are constants) and where only the density contains disorder. The equation for the reflection process simplifies to an equation identical to (3.3), noting that $m^\varepsilon = n^\varepsilon$ and that the nonnegative travel time is computed with a unit speed c_0.

In the ensemble–averaging limit we have shown that the reflection process R^ε for acoustic waves is governed by the same stochastic differential equation as the reflection process Z_{00} for long waves of linear potential theory. The random coefficient is denoted by m^ε and $m(x)$ respectively. In the regime considered, non-hydrostatic effects have disappeared after ensemble–averaging. This is true in the long wave limit, despite of the large amplitude of the topography and despite of the fact that the shallow water equations are not the correct (standard) approximation, at the level of equations.

To make the discussion in this section self–contained, we show the equivalence between the acoustic problem above and the *shallow water model*

$$\frac{\partial u}{\partial t} + g\frac{\partial \eta}{\partial x} = 0 \tag{3.5}$$

$$\frac{\partial \eta}{\partial t} + \frac{\partial (hu)}{\partial x} = 0.$$

It is established as follows. Define $\Psi(x,t) = h(x)u(x,t)$, the variable propagation speed as $c_0(x) = (gh(x))^{1/2}$ and consider

$$t' = \frac{t}{L/c_0(x)}, \quad x' = \frac{x}{L},$$

where L is some characteristic length. Dropping the primes, the shallow water system can written as

$$c_0^{1/2}\frac{\partial \Psi}{\partial t} + c_0^{-1/2}\frac{\partial \eta}{\partial x} = 0 \tag{3.6}$$

$$c_0^{-1/2}\frac{\partial \eta}{\partial t} + c_0^{1/2}\frac{\partial \Psi}{\partial x} = 0.$$

Right and left propagating disturbances are defined by

$$A^+(x,t) = c_0^{-1/2}\Psi + c_0^{1/2}\eta \tag{3.7}$$

and

$$A^-(x,t) = -c_0^{-1/2}\Psi + c_0^{1/2}\eta. \tag{3.8}$$

By using the system above we derive evolution equations for these disturbances. Namely

$$\frac{\partial A^+}{\partial x} + \frac{\partial A^+}{\partial t} = -r(x)A^- \tag{3.9}$$

$$\frac{\partial A^-}{\partial x} - \frac{\partial A^-}{\partial t} = -r(x)A^+,$$

where

$$r(x) = -\frac{1}{2}\frac{d}{dx}\ln(c_0(x)). \tag{3.10}$$

Note that these equations decouple when the medium is homogeneous (i.e. a flat topography).

For the acoustic equations (c.f. Berlyand & Burridge 1994) similar changes of variables can be made, the major difference being the definition of the right and left propagating disturbances:

$$B^+(x,t) = \zeta^{1/2}u + \zeta^{-1/2}p \tag{3.11}$$

and

$$B^-(x,t) = -\zeta^{1/2}u + \zeta^{-1/2}p, \tag{3.12}$$

with the impedance defined by $\zeta(x) = (\rho K)^{1/2} = c_0\rho$. The acoustic propagation speed is $c_0 = (K/\rho)^{1/2}$. The coupled system is

$$\frac{\partial B^+}{\partial x} + \frac{\partial B^+}{\partial t} = -r(x)B^-$$

$$\frac{\partial B^-}{\partial x} - \frac{\partial B^-}{\partial t} = -r(x)B^+,$$

where

$$r(x) = \frac{1}{2}\frac{d}{dx}\ln(\zeta(x)).$$

These equations are identical to those for A^+ and A^-. Hence the shallow water *reflection–transmission model* is equivalent to the corresponding potential theory reflection–transmission problem if we let $h(x) = (1 + m(x))/\gamma_h$. As mentioned in the begining of this section, the smooth coefficient $m(x)$ and the depth parameter γ_h are the only aspects that would not have been captured had one used the shallow water equations directly. This is the argument that led to equations (50)–(52) in Nachbin & Papanicolaou (1992b).

To conclude this section we point out that, in the presence of rapidly varying topographies, a hydrostatic model is not the correct (standard) asymptotic approximation at the level of equations. This is why we referred to it as a *model.* Nevertheless the hydrostatic model captures the correct pulse-rapid-topography interaction and is the correct asymptotic approximation for the reflection–transmission problem in an ensemble–averaging sense. A heuristic explanation can be given by animating the free surface profile of a computational experiment. As the pulse propagates over a rapidly varying topography it vibrates a little bit. The overall impression is that the water is not being vertically accelerated. This is an interesting point to be investigated, in the future, with a non-hydrostatic model. If the steep topography varies on a scale that is not short enough, then the fluid might be vertically accelerated and this heuristic explanation definitely breaks down.

In this paper we will show that the hydrostatic Navier–Stokes model, presented in the next section, is a very useful tool on shedding some light regarding nonlinear waves and viscosity effects. We will start by computationally validating the discussion presented in this section. Another important advantage is the fact that a computationally efficient scheme has been derived by Casulli & Cheng (1992). The efficiency of their semi–Lagrangian, semi–implicit scheme heavily depends on the fact that the pressure term is hydrostatic. We should note that a complete non-hydrostatic study is of great interest, but there is still some work to be done in this direction.

4. The hydrostatic Navier–Stokes model

The starting point for this model are the 3D, primitive variable Navier–Stokes equations describing constant density, free surface flows of an incompressible fluid. The conservation of momentum equations are

$$u_t + uu_x + vu_y + wu_z = -p_x + \mu(u_{xx} + u_{yy}) + \nu u_{zz} \tag{4.1}$$

$$v_t + uv_x + vv_y + wv_z = -p_y + \mu(v_{xx} + v_{yy}) + \nu v_{zz} \tag{4.2}$$

$$w_t + uw_x + vw_y + ww_z = -p_z + \mu(w_{xx} + w_{yy}) + \nu w_{zz} - g. \tag{4.3}$$

The conservation of mass equation is

$$u_x + v_y + w_z = 0. \tag{4.4}$$

The horizontal x and y velocity components are $u(x, y, z, t)$, $v(x, y, z, t)$ and the z–vertical component is $w(x, y, z, t)$. Time is denoted by t, the normalized pressure by $p(x, y, z, t)$ (i.e. normalized by the constant density), the acceleration due to gravity by g and the horizontal and vertical viscosity coefficients by μ and ν, respectively.

Integrating the continuity equation (4.4) over the depth (from the bottom topography $z = -h(x, y)$ up to the free surface $z = \eta(x, y, t)$) we obtain the following free surface condition in conservative form:

$$\eta_t + \left[\int_{-h}^{\eta} u dz\right]_x + \left[\int_{-h}^{\eta} v dz\right]_y = 0. \tag{4.5}$$

This calculation is exact and is obtained by applying the kinematic condition

$$\eta_t + u\eta_x + v\eta_y = w$$

along the free surface and the impermeability condition

$$uh_x + vh_y + w = 0$$

along the bottom. Details of this formulation can be found in Casulli & Cheng (1992).

A shallow water model is derived by adopting the hydrostatic pressure approximation

$$p(x, y, z, t) \approx p_a(x, y, t) + g\left[\eta(x, y, t) - z\right].$$

Without loss of generality, the atmospheric pressure p_a is assumed to be zero. The hydrostatic approximation is commonly used in shallow water ocean, or atmospheric, models. The vertical convection and diffusion terms are neglected, and the final form for the system of partial differential equations to be solved is given by

$$u_t + uu_x + vu_y + wu_z = -g\eta_x + \mu(u_{xx} + u_{yy}) + \nu u_{zz} \tag{4.6}$$

$$v_t + uv_x + vv_y + wv_z = -g\eta_y + \mu(v_{xx} + v_{yy}) + \nu v_{zz} \tag{4.7}$$

$$\eta_t + \left[\int_{-h}^{\eta} udz\right]_x + \left[\int_{-h}^{\eta} vdz\right]_y = 0. \tag{4.8}$$

The vertical velocity component w is calculated from the conservation of mass equation. We will refer to the system above as the hydrostatic Navier–Stokes model (HNS model). Further conditions can be incorporated, such as for the tangential boundary stress along the free surface and along the sediment–water interface (Casulli & Cheng 1992). We omit these conditions since they are not going to be taken into account in our experiments.

The 3D equations above are discretized and solved by a semi–implicit, semi–Lagrangian technique which accomplishes the objective that the stability of the scheme does not depend on the celerity. Based on a linear stability analysis with a two–dimensional shallow water model Casulli & Cheng (1992) derived a scheme which treats implicitly the hydrostatic pressure gradient term, the velocity terms in the free surface evolution equation and the vertical diffusion terms. The reason for treating (only) the vertical viscous term implicitly is that in shallow water applications the ratio of the vertical length scale to the horizontal length scale is very small. Hence the horizontal dissipation rate (i.e. the eddy viscosity) is much smaller than the vertical one. Horizontal dissipation can be of the order of the numerical dissipation, and is therefore treated explicitly.

The spatial grid consists of rectangular cells centered at (x_i, y_j, z_k) of length Δx, Δy and height Δz^n_{ijk}. This height is interpreted as the thickness of the k-th layer of the 3D grid (c.f. figure 2, where only one layer is represented). Because of the presence of the topography and free surface, this thickness can vary in space and time (indicated by the superscript n). The convection terms are treated in a Lagrangian form, through the discretization of the material derivative $(D/Dt)^n_{ijk}$. A fixed staggered grid is defined on the horizontal planes at the interface between vertical layers. In the simulations we perform the relevant unkowns at mesh points are η^n_{ij} at the top layer and $u^n_{i\pm1/2,jk}$. The numerical transport is performed in an Eulerian–Lagragian manner, relying on the interpolation of the respective grid point values at the backward–characteristic point of departure.

An interesting simplification takes place for the single–layer discretization (c.f. figure 2). In this case the vertical spacing Δz (we omit the indices) is taken large enough so that both the bottom and the free surface fall within the same layer. The algorithm reduces to a semi–implicit, semi–Lagrangian discretization of the two–dimensional vertically averaged equations

$$U_t + UU_x + VU_y = -g\eta_x + \mu(U_{xx} + U_{yy}) \tag{4.9}$$

$$V_t + UV_x + VV_y = -g\eta_y + \mu(V_{xx} + V_{yy}) \tag{4.10}$$

$$\eta_t + [HU]_x + [HV]_y = 0 \tag{4.11}$$

where the vertical averages are defined as

$$U(x,y,t) = \frac{1}{H}\int_{-h}^{\eta} u\ dz, \quad V(x,y,t) = \frac{1}{H}\int_{-h}^{\eta} v\ dz$$

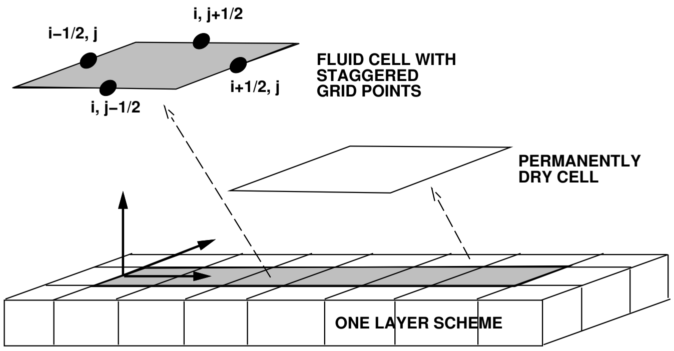

FIGURE 2. Schematic picuture for the one–layer 3D grid.

and $H(x, y, t) = \eta(x, y, t) + h(x, y)$. Details are given in Casulli & Cheng (1992) and the references within. The reduction to a two–dimensional system in the shallow part of the three–dimensional domain contributes to a major improvement in the computational efficiency of the numerical model.

5. Inviscid numerical experiments with linear and nonlinear waves

We performed experiments to observe pulse propagation over different types of topographies. We begin with inviscid experiments in order to compare the results with those of potential theory. Two types of initial conditions were implemented in the hydrostatic code: a mound at rest and a right–going pulse. To illustrate these two conditions consider the linear shallow water equations

$$u_t + g\eta_x = 0,$$

$$\eta_t + h_0 u_x = 0.$$

We call

$$\eta(x, 0) = 2f(x), \quad u(x, 0) = 0, \tag{5.1}$$

the *mound at rest* initial conditions, while

$$\eta(x, 0) = -u(x, 0) = f(x) \tag{5.2}$$

are the *right–going pulse* initial conditions. The factor 2 in the *mound at rest* situation is so that we get two pulses, of a given amplitude and profile, determined by $f(x)$, propagating in opposite directions. We tested both initial conditions with respect to mass conservation after long time intervals and after splashing at the endwalls of a flat channel. The numerical results were satisfactory in both cases. Nevertheless we adopted the *mound at rest* data because it is easier to apply in regions where the topography is varying.

The initial profile in the following experiments are Gaussian pulses of the form

$$f(x) = a\ \exp(-(x - x_0)^2/l_p^2).$$

The dimensionless parameter l_p controls the effective width of the pulse. It will always be chosen so that the effective width is of order one. The rapidly varying features are usually on a scale that is one tenth of the pulse width. Note that in section 2 the microscale was of order one and the pulse width of $O(1/\varepsilon)$. In the computations we focus on the free

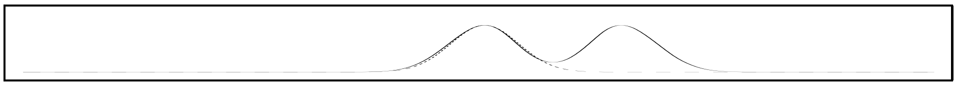

FIGURE 3. Linear regime: $\alpha = 0.001, t = 26units$, no numerical dissipation is observed. The left and right–going pulses are about to collide. The observed amplitude is $a = 1.002$, and the observed numerical speed $c_{num} = 1.018$. The dashed line is the initial condition (halved) and the solid line is the numerical solution.

surface profile setting it to be $O(1)$ with the microscale of $O(\varepsilon)$. It is only the relative ordering in ε that has to be respected.

The amplitude a will be adjusted according to the regime of interest (linear/nonlinear). The propagation speed is always normalized to one.

5.1. *Scaling experiments*

The linear potential theory formulation, presented in section 2, relies on a set of parameters. The first parameter (α) expresses *nonlinearity*. Thus the following questions arise: what is the interval $\alpha \in (0, \alpha_{lin})$ where linear behaviour is *effectively* observed? Will the HNS model respond adequately to these values of α? In order to address these questions we always adjust the numerical model into a dimensionless scenario. Hence, to normalize the wave celerity we change the acceleration due to gravity so that the propagation is speed is always equal to one: $(gh_0) = 1$ or $g = 1/h_0$. We scale in this fashion so that we can also change the values of the amplitude a keeping α fixed. If h_0 is kept fixed, we loose this freedom.

In the first experiment, the initial amplitude of the pulse is $a = 1$. The channel's depth is 1000 and $\alpha = 0.001 = g$. Viscosity is "switched off" and we hope to observe linear advection. After a few calibration experiments, we choose a channel having a total length to 26 units, $\Delta x = 0.01$ and $\Delta t = 0.005$. In the vertical direction we take one layer only and in the y–direction 3 nodes spaced by $\Delta y = 0.1$. The middle node is on the water surface and the two endnodes are on the sidewalls of the channel (c.f. figure 2). Since the data is one–dimensional and the simulation is inviscid, this y–discretization is irrelevant. We will use this philosophy in all experiments of section 5.

The constant, for the implicit scheme, is chosen to be $\theta = 0.5$ (Crank–Nicolson). This value minimizes the numerical dissipation. We run our experiment for 26 units of time. In figure 3 we compare the numerical solution with the *mound at rest* initial condition halved (because the initial data splits into two pulses). Over this time interval, the pulses will go in opposite directions, splash at the endwalls and collide. The exact propagation speed is one. The observed numerical speed is $c_{num} = 0.98$. No numerical dissipation is observed. We are clearly in the *linear advection regime.*

In the experiment presented in figure 4 the same nonlinearity–parameter $\alpha = 0.001$ is adopted. In this experiment the pulse amplitude is $a = 5$ and the depth is $h_0 = 5000$ ($g = 1/5000$). The results presented in figures 3 and 4 are equivalent, meaning that the regime is exactly the same. The code is responding very well to the scaling and hence, to our expectations based on dimensional analysis.

The nonlinearity parameter is now increased by (basically) one order of magnitude ($\alpha = 0.05$). The numerical solution shown in figure 5 is *effectively linear.* Loosely speaking, we will consider a solution to be nonlinear when the wavefront steepens very much or breaks into a bore. This is the case of the experiment that follows. Let the initial amplitude be $a = 1$, the depth be $h_0 = 10$ ($g = 0.1$) and $\alpha = 0.1$. The nonlinearity parameter still has a "small value". The interesting fact is that from the dynamical point of view this value is no longer small. In figure 6 we clearly see that the pulse

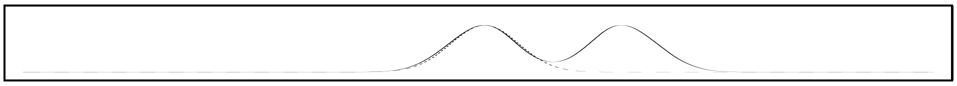

FIGURE 4. Different initial amplitude, $a = 5$, and the same regime as above ($\alpha = 0.001, t = 26 units$). The observed amplitude is $a = 5.017$, and the observed numerical speed $c_{num} = 1.018$. The dashed line is the initial condition (halved) and the solid line is the numerical solution.

breaks and forms a bore. The equations are set on the intermediate wave-scale. Hence a typical long wave has unit width (or O(1) width). According to Burgers equation the characteristic curves will cross at the critical time $t_c = -1/f'(s)$. For the initial condition $f(s) = 0.1\exp(-x^2/0.1)$ we get $t_c = 3.66$.

The ondulations along the front (i.e. the shock) are due to the numerical scheme. The important aspect of this experiment is to realize that Casulli & Cheng's numerical scheme responds well to the scaling.

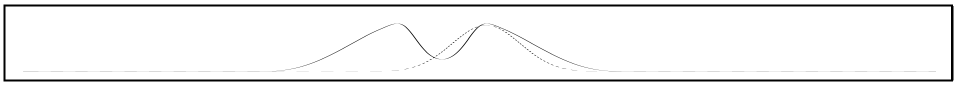

FIGURE 5. Still in the linear regime: $\alpha = 0.005, t = 26 units$ and no numerical dissipation is observed. The left and right–going pulses are about to collide. The dashed line is the initial condition (halved) and the solid line is the numerical solution.

5.2. *Rapidly varying periodic topographies*

In the following set of experiments we considered periodic topographies that are rapidly varying with respect to the pulse width. Usually the ratio (pulse width)/(topography length–scale) is 10/1. A schematic picture is shown in figure 7, which for clarity does not obey the 10/1 ratio.

Consider the periodic topography

$$h(x) = 100. - 50.\ \sin(20\pi x).$$

The background depth is $h_0 = 100$ and the amplitudes of the mean–zero sinusoidal mountains are not small. The initial *mound at rest* is given by the Gaussian water elevation

$$\eta(x, 0) = 2f(x) = 0.2\exp(-x^2/0.1).$$

The shallow water speed is set to $c_0 = 1$ by taking $g = 1/h_0 = 1/100$. Potential theory predicts that the wave will propagate with a speed smaller than 1 and no reflected waves will be observed. The complete nonlinear version of this result is given by Rosales & Papanicolaou (1983). In Nachbin (1993) a straightforward inspection shows that the expression for the *effective shallow water speed* (c.f. appendix) also holds in the linear potential theory regime. The nonlinear hydrostatic model captured this behaviour (figure 8). First we notice that the pulse shape remains practically unchanged as the wave travels over the rapidly varying periodic topography. The small oscillations behind the wave are numerical and disappear very quickly, as seen in the bottom part of figure 8. The observed effective propagation speed is smaller than 1. This is a clear manifestation of a homogenization phenomenon. Since the pulse is broad with respect to the topography's horizontal length scale, it feels the inhomogeneities in an averaged form. The effective propagation speed is somewhat analogous to the effective conductivity of composite materials. Moreover, the homogenization phenomenon is more subtle than just averaging

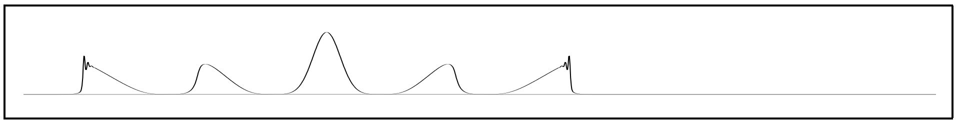

FIGURE 6. Non-linear regime: a bore forms. The parameters are: $\alpha = 0.1$, solution shown at times $t = 0.units, 1.75units$ and $3.5s$.

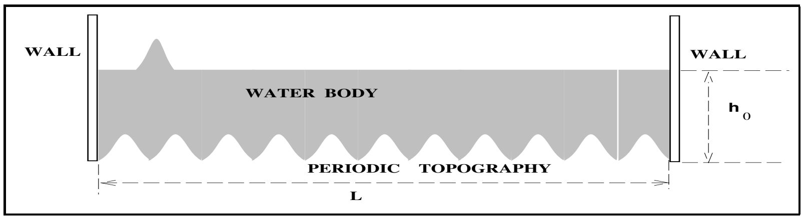

FIGURE 7. Schematic channel with a periodic topography.

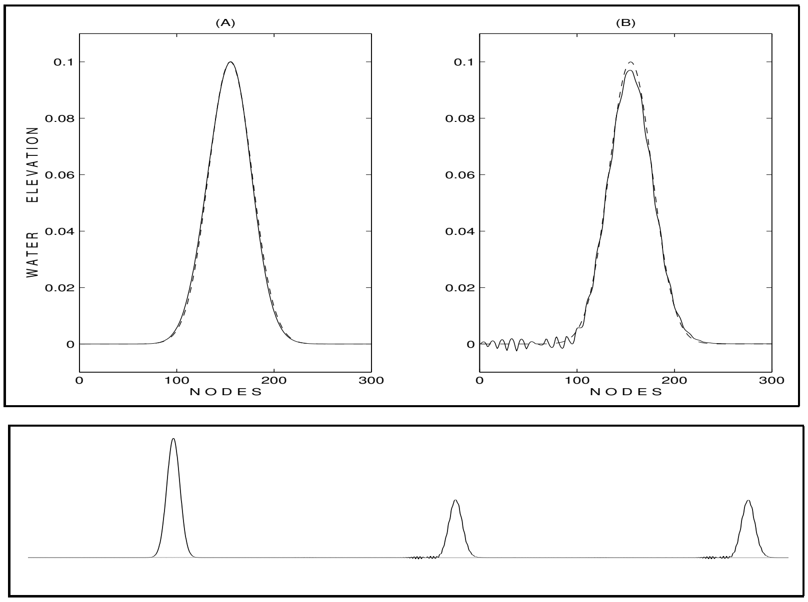

FIGURE 8. **TOP**: Abandoned pulse over **(A)** a flat topography and over **(B)** a (mean zero) rapidly varying topography $(h(x) = 100. - 50.\ \sin(20\pi x))$. The dashed line represents the initial profile for the rightgoing wave. The parameters are: $a = .1, h = 100., \alpha = 0.001, t = 20.0units$, $(\Delta x = 0.01)$, $(\Delta t = 0.0025)$,no numerical dissipation is observed and the numerical propagation speed is $c_{num} = 0.98 \approx 1.$ over the flat topography and $c_{num} = 0.91$ for the periodic case. **BOTTOM**: Relative position with respect to the initial condition. No reflection is observed.

the mean-zero submerged mountains. In figure 9 the same behaviour is observed for a different value of α: no reflection is observed, the propagation speed diminishes and the wave profile is unchanged (c.f. the flat bottom case in figure 5).

For nonlinear breaking waves there is no theory analogous to that presented by Rosales & Papanicoloau (1983). Nevertheless we present qualitative experiments with bores in the presence of a rapidly varying periodic topography. In the top two graphs of figure 10

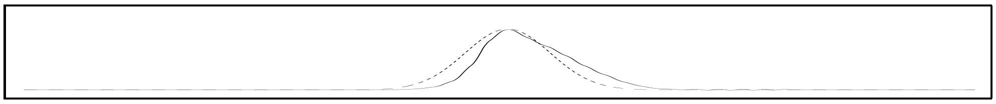

FIGURE 9. Abandoned pulse over periodic topography ($h(x) = 200. - 100.|\sin(20\pi x)|$). Relative position with respect to the initial condition. The parameters are: $a = 1., h = 200., \alpha = 0.005, (\Delta x = 0.01), (\Delta t = 0.0025), t = 21.8units$ and the numerical propagation speed is $c_{num} = 0.8110$.

we see the outgoing nonlinear wave at time $t = 4.0units$ before it breaks. The first case is for a flat channel, while the second is for a periodic one. We clearly see the delay due to the periodic topography. No reflected wave is observed. The bottom two graphs are at a later time ($t = 18.0units$) when the incoming wave has already broken into a bore. We are not aware of any theory for bores in the presence of a rapidly varying environment.

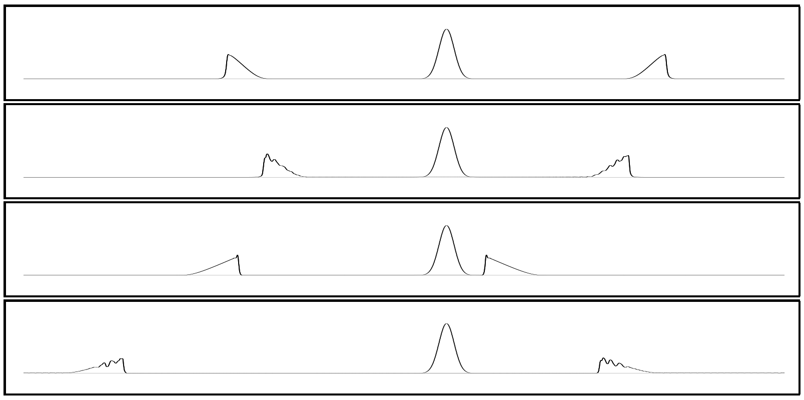

FIGURE 10. The initial condition appears at the center. In the first two figures $t = 4.0$ *units* and the waves are outgoing. In the last two $t = 8.0$ *units* and the waves are incoming, after splashing at the endwalls. From **TOP** to **BOTTOM:** propagation over flat topography ($h(x) = 20$) (first and third figures) and propagation over periodic topography ($h(x) = 20 - 10|\sin(20\pi x)|$; second and fourth figures). The parameters are: $a = 1$, $\alpha = 0.05$, ($\Delta x = 0.01$) total of 2250 steps, $\Delta t = 0.0025$.

It is important to consolidate the *nonbreaking/effective behaviour* of long waves propagating in a rapidly varying channel. In figure 11 we compare the results for four different topographies. The goal of this set of experiments is to show that, even in the presence of large amplitude mountains, the linear regime ($\alpha = 1/200 = 0.005$) is valid, that is, the wave will not break. To give evidence of this fact we compare the results of a flat channel with those of 2 rapidly varying periodic channels in which the mountains' amplitude are 60% and 70% of the total depth. We compute the solution up to 22.4 units of time and superimpose the results. The superposition is done manually since these waves have different (effective) propagation speeds. The wave profiles are practically unchanged (c.f. the dashed and dotted lines in figure 11). It is hard to see three (Gaussian–like) curves since two of them overlap. In all three cases the background depth is $h_0 = 200$ and there is no indication that these waves are in different regimes, because of different mountains' amplitude. Moreover, the summits of these large amplitude mountains will not force the surface waves to break, corroborating linear theory.

A contrasting experiment is devised as follows. First observe that the undisturbed water layer above the summits of the 70%–amplitude mountains is 60 units deep. Consider a flat channel 60 units deep and all other parameters unchanged. Now the parameter α is $1/60 = 0.01666....$ As seen in figure 11 the wave front becomes much steeper for this larger value of α. The wave propagation regime is different from the 3 previous ones. Therefore this experiment confirms that the interaction of surface waves with the upper tips of rapidly varying mountains (which were 60 units deap) will not promote wave-breaking. The effective behaviour applies only to a change in the propagation speed, as a consequence of homogenization theory.

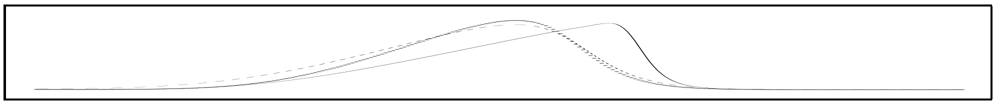

FIGURE 11. Abandoned pulse in 4 different problems (topographies). The fixed parameters are: $a = 1., h = 200., \alpha = 0.005, (\Delta x = 0.01), (\Delta t = 0.0025), t = 22.4 units$. The 4 different topographies considered are: **(A)** $--$ flat bottom, **(B)** $-.-.$ rough $(h(x) = 200. - 120.|\sin(20\pi x)|)$ **(C)** ..... rough $(h(x) = 200. - 140.|\sin(20\pi x)|)$ and **(D) solid** flat bottom $(\alpha = 1./60 = 0.01666)$.

5.3. *Rapidly varying disordered topographies*

This section contains results of Monte Carlo experiments using disordered piecewise-constant topography profiles. The experiments are similar to those presented in Nachbin & Papanicolaou (1992b) and Nachbin (1995), where the potential theory equations were discretized by the boundary element method. Here we make use of the HNS model to generate reflected waves. It is discretized by the semi–implicit, semi–Lagrangian method given in section 4. The reflected signal is recorded at a specified point along the free surface of the channel generating a time history of the water elevation at that point. We compute statistical properties of the reflected signal and compare with theoretical results provided by the potential theory model. Details of the theory are given in Nachbin & Papanicolaou (1992b) and Nachbin (1993). Analogous experiments, for acoustic waves, can be found in Asch *et al.* (1991). As initial conditions they used Gaussian pulses, or its second derivative (Ricker pulses). In Nachbin & Papanicolaou (1992a,1992b) we used Gaussian shaped velocity potentials $\phi(x, 0, 0)$, which give place to water elevation profiles of the form of its first derivative:

$$\eta(x,0) = -2\sqrt{\frac{l_p}{l_b}}(2\pi x)\exp(-4\pi^2 x^2/l_p^2),$$

which is depicted in figure 12.

The expected value for the reflection process (c.f. Asch *et al.* 1991, Nachbin & Papanicolaou 1992b, Nachbin 1995 and equation (A 7)) obtained by the stochastic analysis is

$$E\{R^2(t)\} \;=\; \frac{1}{2\pi}\int_{-\infty}^{\infty} |\hat{f}(\omega)|^2 \; \frac{\omega^2\alpha_{nn}}{[1+\omega^2\alpha_{nn}\; t]^2}\; d\omega,$$

which we repeat here for convenience.

We point out that in the result above, only the correlation function of the random O(1) depth perturbation plays a role in the final result, through the effective parameter for scattering α_{nn} given in (A 8). The mountain profile is given by $n(x)$. The Fourier transform, with respect to the fast variable $\tau = t/\varepsilon$, of the initial pulse shape f is given by

$$\hat{f}(\omega) \;=\; \int_{-\infty}^{\infty} e^{i\omega\tau} f(\tau) d\tau.$$

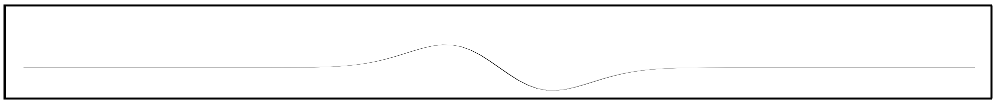

FIGURE 12. Initial condition in the form of the Gaussian's first derivative.

For piecewise–constant disordered topographies, uniformly distributed in $[-\delta, \delta]$, $\delta < 1$, we have that

$$E\{n(x_i+s)n(x_i)\} = \begin{cases} E\{n^2(x_i)\} = \delta^2/3, & \text{for } \ 0 \le s < l_b \\ 0, & \text{for } \ s \ge l_b \end{cases}$$

Hence

$$\alpha_{nn} \;=\; \frac{l_b \delta^2}{3}. \tag{5.3}$$

We can readily calculate the decay in time of the expected value of the reflection process, by Gauss–Hermite numerical integration of

$$E\{R^2(t)\} \;=\; \sqrt{2}\int_{-\infty}^{\infty} \frac{2x^4\alpha_{nn}}{\left[1+2x^2\alpha_{nn}\ t\right]^2}\, e^{-x^2}dx, \tag{5.4}$$

for the derivative of the Gaussian pulse. The corresponding Fourier transforms have been used together with the change of variables $x^2 = \omega^2/2$.

In discretizing the disordered channel we take $\Delta x = 0.01$ and $\Delta y = 0.1$. The mesh has 4500 by 3 nodes and only one vertical layer. The first half of the channel is flat while the second half contains a realization of the piecewise constant topography. The disordered topography fluctuates about 50% ($\delta = 0.5$) of the flat background depth (h_0). The pulse is centered at a point a bit to the left of the disordered topography. The rightgoing pulse will travel over 225 disordered blocks, which compose the bottom profile. We consider $\Delta t = 0.0025$ and perform the time evolution over 16800 time steps (42 units in time). This elapsed time is sufficient for the pulse to travel over the rough channel, splash at the right endwall and propagate back to a point near where we record the reflected signal (i.e. the free surface time history). Note that over this time interval we will not get in the reflected signal any (undesired) indication of the presence of the endwalls. The topography's correlation length is $l_b = 0.05$ and the pulse width is $l_p = 1$. This determines the initial profile's amplitude. We take the undisturbed depth to be $h_0 = 4000$ so that we are in the linear regime, when $\alpha < 1/(4000\sqrt{0.05}) \approx 0.001$. The result of the Monte Carlo simulation is presented in figure 13. For the theoretical curves we used $\alpha_{nn} = 0.5^2 \cdot l_b/3 = 0.0041667$. We observe excellent agreement between theory and computations with only 20 realizations. Each realization takes about 7 minutes on the SGI/Octane R10000. If we had used more realizations the fluctuations from the experimental curve would diminish, as observed in the previous work (Nachbin 1993).

The intense wave/topography interaction, or analogously, the strong stratigraphic filtering of the pulse's spectrum, promotes a quick alignment between the level of the theoretical curve and the results from the Monte Carlo simulation. We refer to Berlyand & Burridge's (1994) article on acoustic waves for more information on the notion of a stratigraphic filter. This filtering is reminescent of the localization phenomenon described in Nachbin & Papanicolaou (1992b). Obviously a pulse with a broader spectrum has a higher wavenumber content. This is the case of the Ricker pulse. The higher part of the spectrum has a shorter localization length (c.f. Nachbin & Papanicolaou 1992b, Devillard *et al.* 1988). Hence they are filtered at a faster rate.

In our next experiment we use the same pulse/inhomogeneities ratio (i.e. $\varepsilon = 0.05$)

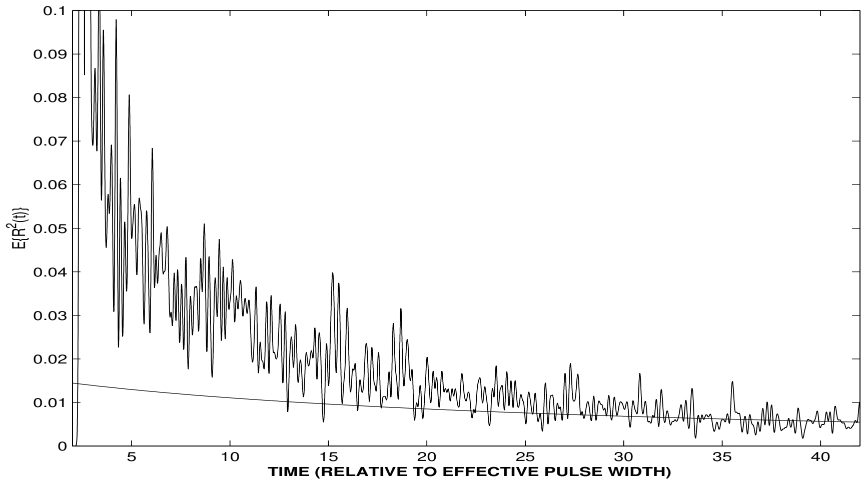

FIGURE 13. Monte Carlo simulation for a pulse width $l_p = 1$: theoretical curve is given by the smooth line and the numerical result was obtained with 20 realizations.

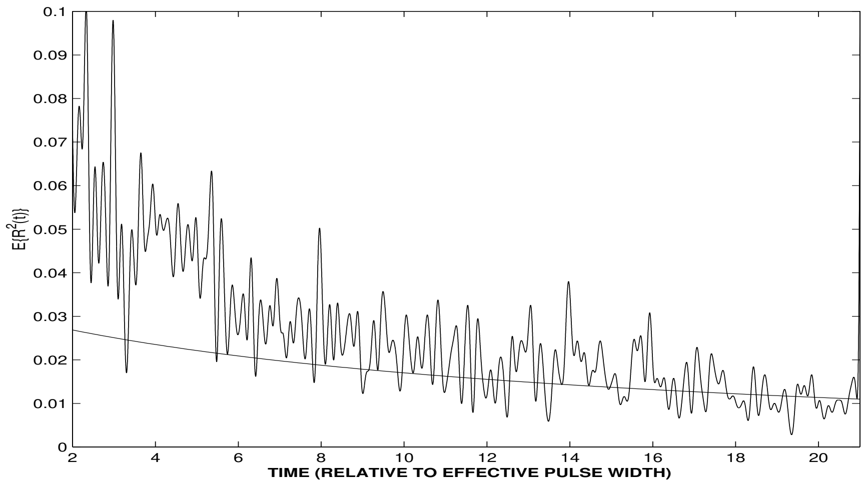

FIGURE 14. Monte Carlo simulation for a pulse width $l_p = 2$: the theoretical curve is given by the smooth line and the numerical result was obtained with 20 realizations.

but with a broader pulse ($l_p = 2$ and $l_b = 0.1$). We have $\alpha_{nn} = 0.5^2 \cdot 0.1/3 = 0.00833$. The space and time discretizations are the same as above. The result is presented in figure 14. The stochastic theory used in Nachbin & Papanicolaou (1992b) makes use of a windowed reflection process centered about the pulse. The length of the window scales with the pulse width and so does the time variable in equation (A 7). This explains why the time axis in figure 14 runs only up to half of our experiment's time interval. It has been scaled by 2, the width of the initial pulse. Again with 20 realizations we observe an excellent agreement between the theory and the Monte Carlo experiment.

To explore the range where the linear asymptotic stochastic theory applies, the parameter α is allowed to vary during a sequence of experiments. The data, geometry and discretization parameters are exactly the same as in the experiment corresponding to

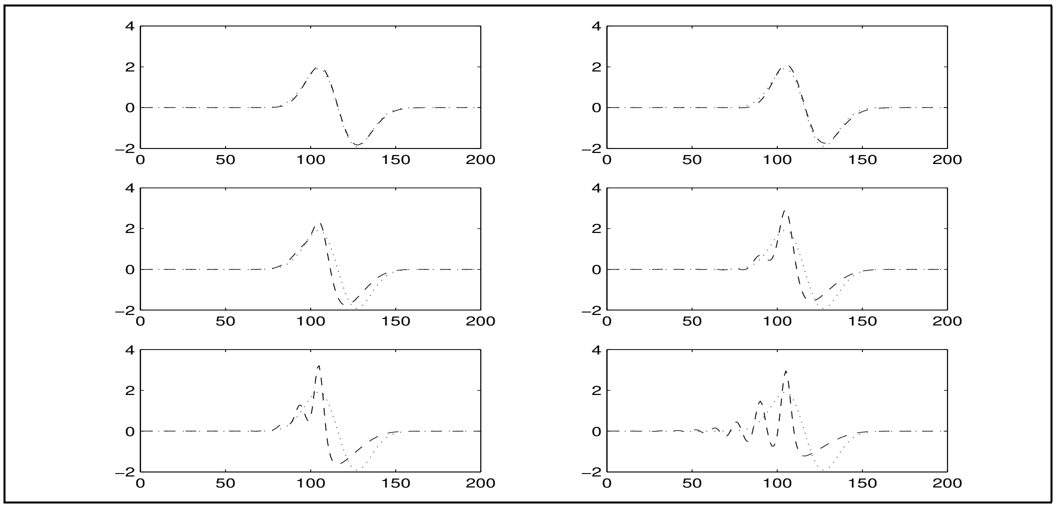

FIGURE 15. The left column represents the solutions at time $t = 8$ *units*, while the right column at time $t = 15$ *units*. The dotted lines represents the initial profile. From top to bottom: $\alpha \approx 0.00025$, $\alpha \approx 0.004$ and $\alpha \approx 0.01$.

figure 13. The only modification regards different choices for the background depth h_0, and therefore different values for α. The initial pulse profile is given by the derivative of a Gaussian, having amplitude $a = 1.93$. The choices for the background depth are such that $\alpha \approx 0.00025$, $\alpha \approx 0.004$ and $\alpha \approx 0.01$ respectively. The difference between each regime is clearly seen in figure 15. The left column represents the solutions at time $t = 8$ *units*, while the right column at time $t = 15$ *units*. The $(\alpha \approx 0.01)$–solution is clearly beyond the linear advection regime.

The expression provided by the stochastic theory (equation (5.4)) is applied to Monte Carlo simulations for all three cases. The results are presented in figure 16. The agreement is very good in all three cases. Only in the third case, at later times, the theoretical curve is slightly above the experimental curve. From figure 16 it is very difficult to tell if the three Monte Carlo curves exhibit different patterns. Figure 17 presents a closer view over a small time interval. The reflected signal has more detailed structure as the solution goes beyond the linear regime. One possible explanation for this fact comes by thinking in terms of the Fourier decomposition of the solution. As the pulse front steepens, its wavenumber content increases. Thus the fine details of the disordered topography are better resolved by the steepening pulse and consequently the reflected signal has more structure.

6. Viscous numerical experiments

When a pulse propagates over a disordered medium it is progressively attenuated, as will be shown below. There is no dissipation in the model. The attenuation is entirely due to multiple scattering and, therefore, is called *apparent attenuation* in the geophysics literature (Richards & Menke 1983). We can also call it *apparent diffusion* due to its connection with a diffusion approximation. This is explained by the O'Doherty–Anstey approximation (O'Doherty & Anstey 1971). Recent work by Clouet & Fouque (1994) and Lewicki *et al.* (1994) show that as an acoustic pulse propagates over large distances, in a disordered stratified medium, the wavefront appears to diffuse as a result of a determinis-

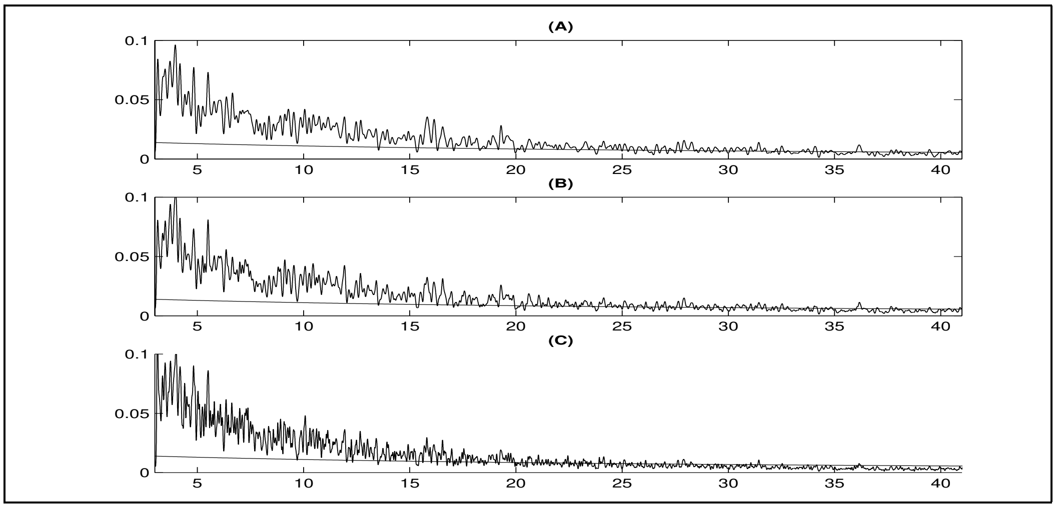

FIGURE 16. Monte Carlo simulations for three different regimes. The theoretical curve is given by the smooth line. The numerical results were obtained with 20 realizations each. From top to bottom: $\alpha \approx 0.00025$, $\alpha \approx 0.004$ and $\alpha \approx 0.01$.

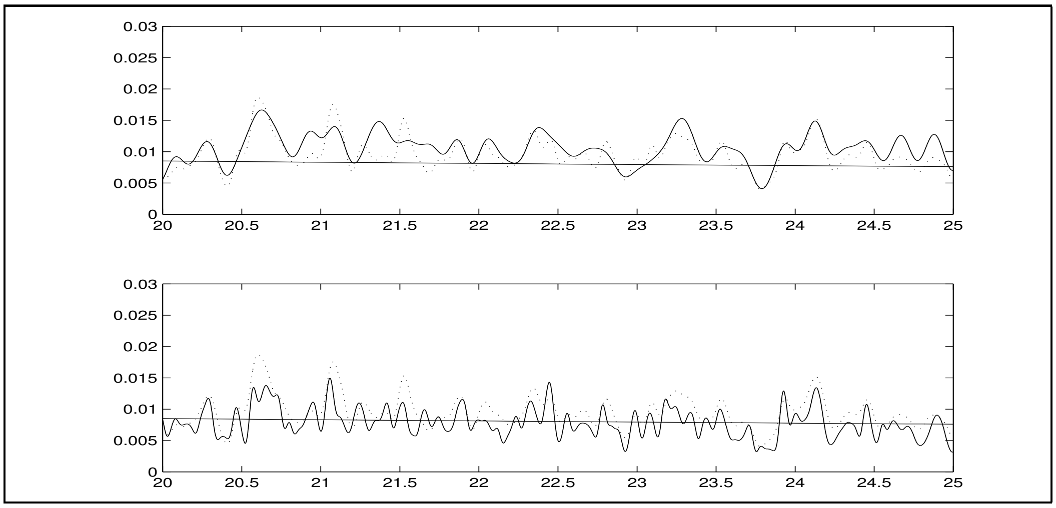

FIGURE 17. Detail of the results from figure 16. Top: $\alpha \approx 0.00025$ (solid line) and $\alpha \approx 0.004$ (dotted line). Bottom: $\alpha \approx 0.004$ (dotted line) and $\alpha \approx 0.01$ (solid line).

tic Gaussian convolution with the initial pulse. In Fourier space this amounts to say that the transmitted pulse is given as a Gaussian (stratigraphic) filter of the initial profile. The energy filtered is contained in the reflected signal, since the system is conservative. The Gaussian kernel resembles a heat kernel hence justifying the terminology presented above. It should be noted that in the O'Doherty–Anstey theory, time and space have roles which are reversed from those of usual diffusion. Apparent diffusion evolves with respect to propagation distance, rather than time (Clouet & Fouque 1994; Lewicki *et al.* 1994).

The O'Doherty–Anstey theory is readily applicable to linear shallow water equations since these are analogous to the linear acoustic equations. In this section the diffusive

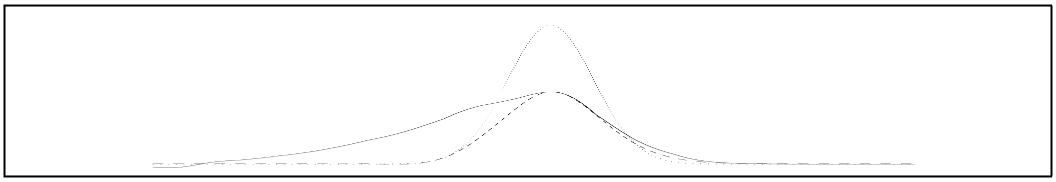

FIGURE 18. The dotted line represents the initial profile for the rightgoing pulse. The dashed line is the numerical solution with viscosity ($\mu = 10^{-4}$) and the solid line is the numerical solution in the presence of a disordered topography. Both numerical solutions are at $t = 50$ units of time. The piecewise–constant disordered topography has $\delta = 0.3$ and $l_b = 0.1$.

effect of viscosity is compared with the apparent diffusion generated by the disordered topography. Devillard *et al.* (1988) have pointed out that there is a band of wavenumbers for which the typical viscous dissipation length is larger then the localization length. Hence apparent diffusion can dominate viscous diffusion. The goal of our first experiment is to give numerical evidence of this fact. Recall that numerical diffusion is kept at a negligible level.

We start by "switching on" the horizontal diffusion term in the HNS model. In Dean & Dalrymple (1991, pp. 262) the Reynolds number, for normal ocean waves, is defined as $R_e = \omega k^{-2}/\mu$, where ω is the frequency, k the wavenumber and μ the horizontal kinematic viscosity coefficient. The regime for these waves is given as $R_e^{-1} = O(10^{-7} - 10^{-8})$. We set $\mu = 10^{-4}$ and $\nu = 0$ in equations (4.9)-(4.10). The discretization parameters are $\Delta x = 0.01$, $\Delta y = 0.1$ and $\Delta t = 0.0025$. The amplitude of the rightgoing Gaussian pulse is $a = 0.2$ and $\alpha = 0.001$. The pulse's effective width is equal to 1. The channel is 80 units long and we allow the pulse to propagate for 50 units of time. The numerical solution is presented as the dashed line in figure 18.

To contrast the two diffusive effects, we set $\mu = 0$ and generate a realization of a disordered topography with correlation length 0.1 and amplitude 30% of the undisturbed depth. We allow the same Gaussian pulse to propagate for the same time interval. The numerical solution is given by the solid line in figure 18. For this choice of parameters, the two numerical solutions match very well along the wavefront. Hence if we decrease the value of μ, setting it in the interval given in Dean & Dalrymple (1991), it is clear that apparent diffusion will dominate.

In the next experiment we analyze the joint effect of viscosity and disorder. We consider the same set of parameters as in the first Monte Carlo experiment of the previous section. Two values are chosen for horizontal viscosity: $\mu = 10^{-8}$ and $\mu = 10^{-4}$. The results of the Monte Carlo simulations are presented in figure 19. Note that at later times, not only both solutions are below the theoretical (potential theory) curve, but the more viscous solution (with $\mu = 10^{-4}$) is below the less viscous one (with $\mu = 10^{-8}$). In the bottom graph of figure 19 we performed a close–up along the later time interval. We observe that if the viscosity is weak enough, the theorical curve could be adjusted by a translation, indicated by the dashed line. Thus the rate of decay of the reflection coefficient is preserved. Nevertheless for the second case the slopes do not match anymore. The problem of understanding the combined effect of viscosity and disorder is very interesting and needs further investigation.

7. Conclusions

We have considered linear potential theory as a reduced/prototypical model for water wave propagation. We have shown that results obtained previously (Nachbin & Papan-

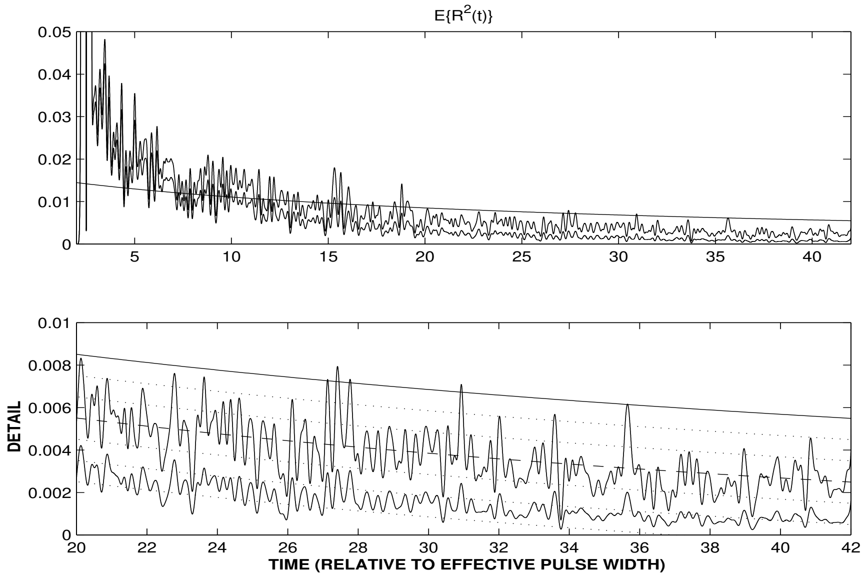

FIGURE 19. Joint effect of viscosity and disorder. **TOP**: viscous Monte Carlo experiments with $\mu = 10^{-8}$ and $\mu = 10^{-4}$. Solution for $\mu = 10^{-4}$ has more decay in time. **BOTTOM**: Detail of above. The solid line is the theoretical curve, below it the ($\mu = 10^{-8}$)–solution and finally the ($\mu = 10^{-4}$)–solution.

icolaou 1992a, 1992b, Nachbin 1995) persist under a more complete nonlinear model. The validation results make use of both periodic and disordered topographies. One very important result relates to nonlinear wave breaking. We show that long waves in the presence of large amplitude rapidly varying topographies do not break. This corroborates linear theory. The underlying theme is effective media. The long waves feel the medium in an averaged form. The form through which this takes place is more complicated than just averaging coefficients of the governing equation. For example there is a dramatic difference between periodic and disordered irregularities, where homogenization theory can not account for the apparent diffusion promoted by disordered multiple scattering.

Succeeding with the validation results we explored new regimes beyond linear potential theory. Nonlinear wave propagation over rapidly varying topographies was considered. In particular we showed the delay of bores propagating over periodic topographies. We also showed how a small amount of viscosity can affect the linear potential theory results for the reflection–transmission problem. Hopefully these results will stimulate the production of new theories in this field.

I would like to thank Vincenzo Casulli in a special way. First for showing me how to use TRIM3D (his 3D hydrostatic Navier–Stokes code) and for helping me adjust it to my experiments. Also for his generosity and hospitality during my visit to the Università di Trento, Italy. I also want to thank George Papanicolaou for fruitful discussions.

This work was supported in part by: CNPq under Grant 300368/96-8; CNPq under Grant CNPq/NSF 910029/95-4; FAPERJ under Travel Grant E-26/170.513/96; and NEC/CEMAT under Grant DMS 2.419/98-00.

Appendix A. Summary of results from potential theory

We briefly present the potential theory results, to be verified with the hydrostatic Navier–Stokes model.

A.1. *Results from the multiscale analysis of periodic channels*

Rosales & Papanicolaou (1983) analyzed the nonlinear set of equations of §2, in the case where the topography is periodic. In their asymptotic analysis a multiscale *ansatz* is considered for both the velocity potential and the water elevation:

$$\phi(x,z,t) = \phi_0(\chi,\xi,z,\tau) + \sqrt{\varepsilon}\phi_1(\chi,\xi,z,\tau) + \varepsilon\phi_2(\chi,\xi,z,\tau) + ...$$

$$\eta(x,t) = \eta_0(\chi,\xi,\tau) + \sqrt{\varepsilon}\eta_1(\chi,\xi,\tau) + \varepsilon\eta_2(\chi,\xi,\tau) + ...$$

In the above expansions $\tau = \varepsilon t$, $\chi = x - Ct$ and $\xi = x/\sqrt{\varepsilon}$. Thus the *ansatz* means that the rightgoing wave has an effective propagation speed of C (to be determined); it can change slowly in time τ and it can have rapidly varying periodic dependence on ξ, due to the topography. The problem is scaled so that $h(\xi+1) = h(\xi)$ with parameters $\alpha = O(\varepsilon)$, $\beta = \beta_0\varepsilon$ and $\gamma = \sqrt{\varepsilon}$.

When the expansions are substituted into the potential theory equations, a sequence of cell–problems emerge, ordered by the powers of ε. A cell is defined by $0 < \xi < 1$ and $-h(\xi) < z < 0$. A typical cell–problem has the form

$$\beta_0\phi_{j\xi\xi} + \phi_{jzz} = a(\xi,z), \quad \text{in } -h(\xi) < z < 0, \quad j = 0,1,2,... \tag{A 1}$$

$$\phi_{jz} + \beta_0 h_\xi \phi_{j\xi} = b(\xi), \quad \text{on } z = -h(\xi),$$

and

$$\phi_{jz} = c(\xi), \quad \text{on } z = 0.$$

The forcing terms are periodic functions of ξ and the ϕ_j's are to be periodic also. This sequence of linear elliptic problems has a corresponding compatibility condition to be satisfied. For the $O(\varepsilon)$–equations the compatibility condition leads to the expression

$$C^2 = 1 - \int_0^1 \int_{-h(\xi)}^0 \left(A_\xi^2(\xi,z) + \beta_0^{-1}A_z^2(\xi,z)\right) dz d\xi < 1. \tag{A 2}$$

The auxiliary function $A(\xi,z)$ solves an elliptic problem, as given by equations (A 1), with $a = c = 0$ and $b(\xi) = -\beta_0 h_\xi$. The effective (delayed) speed is given by equation (A 2).

We have verified that in the linear case expression (A 2) has the same form. There are two points in the analysis that should be highlighted. First, the leading term (ϕ_0) in the potential expansion does not depend on ξ. Also, backscattering is being ignored in the formulation by accounting only for rightgoing waves. Through numerical experiments these points are substantiated. We show the delay of linear and nonlinear long waves propagating over large amplitude periodic topographies. We also show that backscattering is negligible and that the wave profile is effectively unchanged. We also present new results of exploratory nature, beyond the validity of the theory of Rosales & Papanicolaou (1983). Namely, we observe the behaviour of bores in the presence of a periodic topography.

A.2. *Results from the analysis of stochastic differential equations*

This section contains a brief summary of the results obtained in Nachbin & Papanicolaou (1992b) and Nachbin (1995). The problem studied in Nachbin & Papanicolaou (1992b) is linear ($\alpha = 0$). In order to formulate the reflection-transmission problem it is convenient to conformally map the rough channel onto a flat one. A system of stochastic differential equations is derived for the amplitudes of the propagating and evanescent modes, obtained from the eigenfunction decomposition of the time-harmonic velocity potential. The solution to these equations is characterized asymptotically as a diffusion process through the application of a limit theorem for stochastic differential equations. This allows the characterization of the expected value of the transmission or reflection coefficient. Details of the stochastic theory can be found in Asch *et al.* (1991) and references therein.

Consider a channel having a disordered topography varying on a length scale caracterized by l_b. We start with the time–harmonic results in order to define the basic concepts and notation. The expected value of the transmission coefficient, for an incident monochromatic wavetrain of frequency ω, is given as

$$E\{|T|^2\} \;=\; exp\left(-\frac{\gamma_L\ \omega^2}{8\gamma_h^2}\alpha_{mm}\right)\ \int_{-\infty}^{\infty} exp\left(-t^2\frac{\gamma_L\ \omega^2}{2\gamma_h^2}\alpha_{mm}\right)\frac{\pi t\ sinh\pi t}{cosh^2\pi t}\ dt.$$

The phenomenon of localization is characterized by the exponential decay of the transmission coefficient as a function of the total length of the rough region, expressed here through the dimensionless parameter γ_L. Localization is the mechanism that accounts for the apparent attenuation observed for pulsed shaped waves propagating in disordered media (Asch *et al.* 1991).

In the expression above the effective parameter for scattering

$$\alpha_{mm} \;=\; \frac{1}{(1+<m>)^2}\ \int_0^{\infty} E\{m_0(s)m_0(0)\}ds \tag{A 3}$$

is known, where $\gamma_h = h_0/l_b$,

$$m(\xi) \;=\; \frac{\pi}{4\gamma_h}\ \int_{-\infty}^{\infty}\frac{n(x(\xi_0,-\gamma_h))}{cosh^2\frac{\pi}{2\gamma_h}(\xi_0-\xi)}d\xi_0, \tag{A 4}$$

and

$$m(\xi) = <m> + m_0(\xi). \tag{A 5}$$

We define the average as

$$<m> = \frac{1}{\gamma_L}\int_{-\gamma_L}^{0} m(\xi)d\xi \tag{A 6}$$

and $m_0(\xi)$ as the mean-zero part. The justification for these expressions, depending on $m(\xi)$, is given in Nachbin (1995).

For the propagation of a pulse we give the expected value for the reflection process (where $E\{R^2(t)\} = 1 - E\{T^2(t)\}$):

$$E\{R^2(t)\} \;=\; \frac{1}{2\pi}\int_{-\infty}^{\infty}\ |\hat{f}(\omega)|^2\ \frac{\gamma_h\omega^2\alpha_{mm}}{\left[\gamma_h+\omega^2\alpha_{mm}\ t\right]^2}\ d\omega.$$

The initial pulse shape $\phi_t(x,0,0) = \eta(x,0) = f(x)$ is known and its Fourier transform given by

$$\hat{f}(\omega) \;=\; \int_{-\infty}^{\infty} e^{i\omega\tau}f(\tau)d\tau.$$

The decay in time of the expected value of the reflection process is given by the numerical Gauss–Laguerre integration of the expression above.

To facilitate to the application of these results to the hydrostatic Navier–Stokes model, lets consider directly the discretized (piecewise constant $n(x)$) topography with $\gamma_h = 1$. Consequently $\alpha_{mm} \approx \alpha_{nn}$ and

$$E\{R^2(t)\} \;=\; \frac{1}{2\pi}\int_{-\infty}^{\infty} |\hat{f}(\omega)|^2 \; \frac{\omega^2\alpha_{nn}}{\left[1+\omega^2\alpha_{nn}\; t\right]^2}\; d\omega \qquad \text{(A 7)}$$

with

$$\alpha_{nn} \;=\; \int_0^{\infty} E\{n(s)n(0)\}ds. \qquad \text{(A 8)}$$

We explore the results above, using the nonlinear hydrostatic Navier–Stokes model.

REFERENCES

ASCH M., KOHLER W., PAPANICOLAOU G., POSTEL M. & WHITE B., 1991, Frequency content of randomly scattered signals, *SIAM Review*, **Vol. 33**, pp. 519–625.

BELZONS, M., GUAZZELLI, E. & PARODI, O., 1988, Gravity waves on a rough bottom: experimental evidence of one-dimensional localization, *J. Fluid Mech.*, **Vol. 186**, pp. 539–558.

BERLYAND, L. & BURRIDGE, R., 1995, The accuracy of the O'Doherty-Anstey approximation for wave propagation in highly disordered stratified media, *Wave Motion*, **21**, pp. 357–373.

BURRIDGE, R., PAPANICOLAOU, G.C., SHENG, P. & WHITE, B. 1989, Probing a random medium with a pulse, *SIAM J. Appl. Math.*, **49**, pp. 582–607.

CASULLI, V., & CHENG, R.T., 1992, Semi-implicit finite difference methods for three-dimensional shallow water flow, *Int. J. Num. Meth. Fluids*, vol. 15, pp. 629–648.

CLOUET, J.F. & FOUQUE, J.P., 1994, Spreading of a pulse travelling in random media, *Ann. Appl. Probability*, **Vol. 4**, No. 4, pp. 1083–1097.

DEAN, R.G. & DALRYMPLE, R.A., 1991, *Water Wave Mechanics for Engineers and Scientists*, World Scientific.

DEVILLARD, P., DUNLOP, F. & SOUILLARD, B., 1988, Localization of gravity waves on a channel with a random bottom, *J. Fluid Mech.*, **vol. 186**, pp. 521–538.

EVANS, D.V., & LINTON, C.M., 1994, On step approximations for water wave problems, *J. Fluid Mech.*, **vol. 278**, pp. 229–249.

LEWICKI, P., BURRIDGE, R. & PAPANICOLAOU, G.C., 1994, Pulse stabilization in a strongly heterogeneous layered medium, *Wave Motion*, **20**, pp. 177–195.

MEI, C.C., 1983, *The Applied Dynamics of Ocean Surface Waves*, John Wiley.

NACHBIN, A. 1993, *Modelling of Water Waves in Shallow Channels*, Computational Mechanics Publicactions, Southampton, U.K.

NACHBIN, A. 1995, The localization length of randomly scattered water waves, *J. Fluid Mech.*, **Vol. 296**, pp. 353–372.

NACHBIN, A. & PAPANICOLAOU, G.C. 1992a, Boundary element method for the long-time water wave propagation over rapidly varying bottom topography, *Intern. J. Num. Meth. in Fluids*, **Vol. 14**, pp. 1347–1365.

NACHBIN, A. & PAPANICOLAOU, G.C. 1992b, Water waves in shallow channels of rapidly varying depth, *J. Fluid Mech.*, **Vol. 241**, pp. 311–332.

O'DOHERTY, R.F. & ANSTEY, N.A., 1971, Reflections on amplitudes, *Geophysical Prospecting*, **19**, pp. 430–458.

REY, V., BELZONS, M. & GUAZZELLI, E. 1992, Propagation of surface gravity waves over a rectangular submerged bar, *J. Fluid Mech.*, **Vol. 235**, pp. 453–479.

RICHARDS, P.G. & MENKE, W. 1983, The apparent attenuation of a scattered medium, *Bull. Seism. Soc. America*, **73**, pp. 1005–1021.

ROSALES, R.R. & PAPANICOLAOU, G.C. 1983, Gravity waves in a channel with a rough bottom, *Studies in Appl. Math.*, **68**, pp. 89–102.

WHITHAM, G.B. 1974, *Linear and Nonlinear Waves*, John Wiley.